Normal Force Elimination in Single-Sided Linear Induction Motor Using Design Parameters

Abbas Shiri, *Member, IEEE*, and Alberto Tessarolo, *Senior Member, IEEE*

***Abstract*— In this article, the normal force acting on the primary of single-sided linear induction motors (SLIMs) is analytically derived. Considering all phenomena involved, the effects of different design variables on the normal force are investigated. In some applications such as transportation systems, the normal force elimination may be required or strongly beneficial, and, in this article, a multi-objective design optimization method based on genetic algorithm is introduced for this purpose, both with and without consideration of primary weight effect. All significant design variables are considered in the optimization. The results show that the motor performance is improved and the normal force is eliminated by an appropriate selection of design variables. To evaluate optimization effectiveness, a laboratory prototype has been constructed, tested, and numerically simulated by finite element analysis (FEA). Comparing the experimental and FEA results with analytical predictions confirms the accuracy and usefulness of the proposed design methodology.**

***Index Terms*— Finite element method, genetic algorithm, normal force, optimization, single-sided linear induction motor.**

Nomenclature

g	Air-gap length.
w_s	Slot width.
w_t	Tooth width.
h_s	Slot height.
h_y	Primary back-iron height.
τ_s	Slot pitch.
R_1	Primary winding resistance.
N	Per-phase number of turns of the primary winding.
X_1	Primary winding reactance.
R'_2	Secondary resistance referred to primary.
R_m	Magnetizing branch resistance representing the power loss due to end effect.
X_{m1}	Modified magnetizing reactance considering end effect.
σ_w	Conductivity of the conductor used in the primary winding.
W_s	Primary width.
l_{ec}	End connection length.
J_1	Primary current density.
μ_0	Permeability of the air (vacuum).
ω_1	Primary angular frequency.
λ_s	Permeance of slot.
λ_d	Differential permeance.
λ_e	Permeance of end connection.
p	Number of pole pairs.
q	Number of slots per pole per phase.
W_{se}	Equivalent primary width.
k_w	Winding factor.
τ	Pole pitch.
σ_{ei}	Modified conductivity of the secondary.
d	Secondary sheet thickness.
Q	Normalized motor length.
g_{ei}	Modified air-gap length.
s	Slip.
f_1	Primary supply frequency.
F_{xo}	Output thrust.
L_s	Primary length.
V_r	Motor speed.
F_x	Produced thrust.
I_m	Magnetizing branch current in equivalent circuit.
I_1	Phase input current.
V_1	Phase input voltage.
Z	Per-phase input impedance.
H	Magnetic field intensity.
E	Electric field intensity.
B	Magnetic flux density.
V_s	Linear synchronous speed.
F_{ya}	Attraction normal force.
F_{yr}	Repulsion normal force.
F_y	Electromagnetic normal force.
F_{yw}	Normal force due to primary weight.
F_{yt}	Total normal force.

I. Introduction

LINEAR motors (LMs) are capable of producing linear motion without any need for transmission system and mechanical gears. Among different kinds of LMs, the linear induction motor (LIM) is popular due to its simple and rugged structure. So, extensive investigation has been carried out on this kind of machines [1]–[5]. There are different types of LIMs and, among them, single-sided linear induction motors (SLIMs) are widely used in transportation systems [6]–[8]. In the literature, many investigations are reported on the design and optimization of LIMs [9]. In [10], the primary weight has been considered as the objective function to achieve an optimal design. In other works, the thrust and power-to-weight ratio

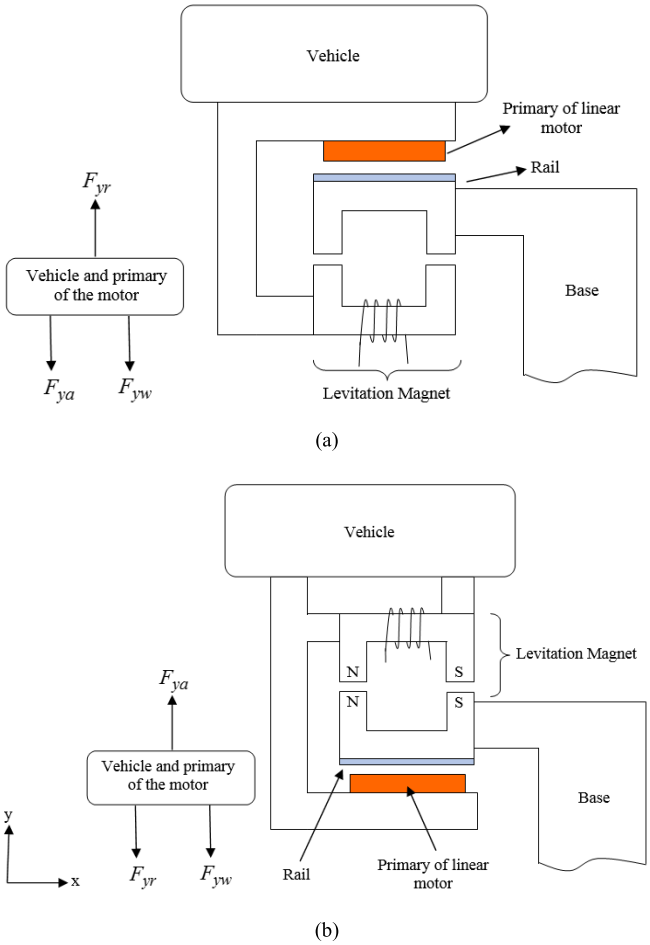

Fig. 1. Two different approaches to SLIM levitation: (a) electromagnetic levitation and (b) electrodynamic levitation.

are maximized [11]. In [12], an optimal winding layout of LIM has been presented. In other researches, optimal LIM design for maximized efficiency and power factor has been proposed [13], [14]. In [15] and [16], the end effect phenomenon has been modeled and included in the design. In particular, normal forces play an important role in SLIMs, especially in high-speed transportation [17], [18], and there are some researches which have investigated and analyzed the issue in detail [19]–[23]. Electromagnetic field methods [24]–[26] and finite element method [27] are usually used to calculate normal forces in SLIMs; however, in recent years, magnetic equivalent circuit techniques have been spreading for thrust and normal force calculations [28].

For transportation applications, especially in magnetic levitation systems, the normal force is usually regarded in SLIMs as a meaningless phenomenon [29]. However, to illustrate its significance, Fig. 1 shows two possible electromagnetic and electrodynamic levitation techniques applied to SLIMs, wherein a short primary SLIM is used in which the secondary is integral with the rail. For both the cases in Fig. 1, along with the normal force applied by the levitation magnet, there are three normal forces acting on the primary: attraction, repulsion, and weight force. These forces act on the primary in different directions as shown in Fig. 1(a) and (b). To reduce

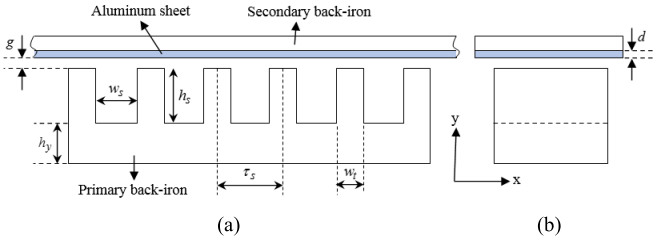

Fig. 2. Structure of SLIM: (a) side view and (b) front view.

the cost of the levitation magnet and improve the levitation process, the motor should be designed in such a way that the three normal forces acting on the primary cancel each other out.

In this article, design equations based on the equivalent circuit model are presented for SLIM. Then, considering all phenomena involved in the motor operation, the effect of different design variables on the normal force and other performance aspecnts are analyzed. Considering all effective design variables, genetic-algorithm-based multi-objective design optimization is proposed to minimize the primary weight and the absolute value of the normal force on it, as well as to maximize the efficiency and power factor. Including the normal force in design optimization and canceling it out to reduce the cost of the levitation magnet and improve the levitation process for different levitation configurations are the main aims and novelties of the current article.

As a case study, an example SLIM is initially designed and optimized and then simulated using FEA. Simulations are then shown to confirm the validity of the proposed design equations and optimization approach. Finally, as a further validation, the designed motor is constructed and tested showing good accordance between the measurements and analytical results.

II. Equivalent Circuit Parameters and Output Equations for SLIM

In the literature, equivalent circuit models have been widely used to study the performance and design of SLIM [30]–[32]. In this article, the optimal design of the SLIM structure sketched in Fig. 2, based on the model presented in [30] and herein recalled, is addressed. The equivalent circuit parameters of SLIM can be written as follows [16], [33]:

$$R_1 = K_{R_1} N^2 \tag{1}$$

$$X_1 = K_{X_1} N^2 \tag{2}$$

$$R_2' = K_{R_2'} N^2 \tag{3}$$

$$R_m = K_{R_m} N^2 \tag{4}$$

$$X_{m1} = K_{X_{m1}} N^2. \tag{5}$$

In the above equations, different coefficients are defined as follows [33]:

$$K_{R_1} = \rho_w \frac{2(W_s + l_{\mathrm{ec}}) J_1}{\mathrm{MMF}_1} \tag{6}$$

$$K_{X_1} = \frac{2\mu_0 \omega_1 \left[\left(\lambda_s \left(1 + \frac{3}{2p} \right) + \lambda_d \right) \frac{W_s}{q} + \lambda_e l_{\mathrm{ec}} \right]}{p} \tag{7}$$

$$K_{R_2'} = \frac{6W_{\rm se}k_w^2}{p\tau\sigma_{\rm ei}d} \tag{8}$$

$$K_{R_m} = K_{R_2'}\left(\frac{1-e^{-Q}}{Q}\right) \tag{9}$$

$$K_{X_{m1}} = \frac{6\mu_0\omega_1 W_{\rm se}k_w^2\tau}{\pi^2 p g_{\rm ei}}\left(1-\frac{1-e^{-Q}}{Q}\right). \tag{10}$$

In (6), (9), and (10), MMF_1 and Q are the magneto-motive force (MMF) required to produce the desired output thrust and normalized motor length, respectively, which can be expressed as follows:

$$\mathrm{MMF}_1 = \sqrt{\frac{s2\tau f_1 F_{xo}}{3K_{R_2'}}\frac{\left(K_{R_2'}/s+K_{R_m}\right)^2+K_{X_{m1}}^2}{K_{R_m}^2+K_{X_{m1}}^2}} \tag{11}$$

$$Q = \frac{L_s K_{R_2'}\omega_1}{V_r\, K_{X_m}}. \tag{12}$$

In addition, the motor efficiency, input power factor, and output thrust are derived as

$$\eta = \frac{F_x 2\tau f_1(1-s)+3(s-1)R_m I_m^2}{F_x 2\tau f_1+3I_1^2R_1} \tag{13}$$

$$\cos\phi = \left[F_x 2\tau f_1+3I_1^2R_1\right]/[3I_1V_1] \tag{14}$$

$$F_{xo} = \frac{3I_1^2R_2'}{s2\tau f_1}\left[\frac{R_m^2+X_{m1}^2}{\left(R_2'/s+R_m\right)^2+X_{m1}^2}\right]. \tag{15}$$

III. SLIM Design

As it is seen from (1) to (5), to calculate the equivalent circuit parameters and design SLIM, the number of turns per phasen should be determined. To this end, one can calculate the per-phase input impedance of the motor as follows (with j and $||$ representing the imaginary unit and parallel operator, respectively):

$$Z = R_1 + jX_1 + (R_m + jX_{m1})\,||\left(R_2'/s\right). \tag{16}$$

Using (1)–(5) in (16) and applying Ohm's law in the single-phase equivalent circuit, the number of turns per phase is derived as

$$N = \sqrt{V_1/(K_z I_1)} \tag{17}$$

where $K_z = Z/N^2$ is a coefficient which is calculated as follows:

$$K_z = K_{R_1} + jK_{X_1} + \left(K_{R_m} + jK_{X_{m1}}\right)||\,(K_{R'2}/s). \tag{18}$$

By deriving the per-phase number of turns from (17), the calculation of the equivalent circuit parameters and other motor outputs is straightforward. The detailed procedure that can be followed for the design process can be found in [16].

IV. Electromagnetic Normal Force Calculation

The Maxwell equations are used in this section to calculate the air-gap magnetic flux density. The basic Maxwell equations in any region are [34]

$$\nabla\times H = \sigma(E+V\times B) \tag{19}$$

$$\nabla\cdot B = 0. \tag{20}$$

In the above equations, V is the speed and σ is the material conductivity. Supposing the conductivity of the air-gap equal to zero, (19) reduces to

$$\nabla\times H = 0. \tag{21}$$

It is assumed that the equivalent current sheet of the SLIM primary has the following distribution over space and time:

$$j_1 = J_m e^{j\left(\omega_1 t-\frac{\pi}{\tau}x\right)} \tag{22}$$

where J_m is calculated as follows:

$$J_m = 3\sqrt{2}NI_1k_w/(p\tau). \tag{23}$$

By applying suitable boundary conditions and assuming a theoretically infinite iron permeability, the air-gap magnetic flux density in the x- and y-directions is derived as per the following equations, (24) and (25), as shown at the bottom of the next page. The time average attraction normal force exerted on the primary (or secondary) of the motor is derived as follows [19]:

$$F_{\rm ya} = \frac{W_s}{4\mu_0}\int_0^{L_s} Re\left[B_yB_y*\right]dx \tag{26}$$

where B_y^* denotes the complex conjugate of B_y. By substituting (25) into (26), after some mathematical manipulations, the attraction normal force is obtained as

$$F_{\rm ya} = \frac{\mu_0 L_s W_s}{4}\frac{J_m^2}{\sinh^2(\pi g_{\rm ei}/\tau)+(\sigma_{\rm ei}d\mu_0 sV_s)^2\cosh^2(\pi g_{\rm ei}/\tau)}. \tag{27}$$

Likewise, the repulsion normal force exerted on the primary (or secondary) is calculated by the following equations [19]:

$$F_{\rm yr} = \frac{W_s}{4\mu_0}\int_0^{L_s} Re[B_xB_x*]dx \tag{28}$$

$$F_{\rm yr} = \frac{\mu_0 L_s W_s}{4}\frac{(\sigma_{\rm ei}d\mu_0 sV_s)^2J_m^2}{\sinh^2(\pi g_{\rm ei}/\tau)+(\sigma_{\rm ei}d\mu_0 sV_s)^2\cosh^2(\pi g_{\rm ei}/\tau)}. \tag{29}$$

So, the net electromagnetic normal force acting on the primary in the y direction is calculated as follows:

$$F_y = \frac{\mu_0 L_s W_s}{4}\times\frac{1-(\sigma_{\rm ei}d\mu_0 sV_s)^2}{\sinh^2(\pi g_{\rm ei}/\tau)+(\sigma_{\rm ei}d\mu_0 sV_s)^2\cosh^2(\pi g_{\rm ei}/\tau)}J_m^2. \tag{30}$$

V. Model Validation Against FEA and Sensitivity Analysis

In this section, the SLIM motor model presented in Sections II–IV for normal force computation is first validated against FEA simulations of a sample motor. Next, a sensitivity analysis is presented to highlight how the motor performance and the normal force acting on the primary depend on some key design variables, as a premise to design optimization.

TABLE I

SPECIFICATIONS OF INITIAL DESIGNED MOTOR

Specification	Values
Primary width, mm	308.3
Secondary sheet thickness, mm	5.1
Air gap length, mm	5
Slip	0.05
Number of pole pairs	2
Frequency, Hz	50
Number of turns per phase, N_1	48
Phase input current, A	185.5
Motor length (L_s), mm	891.2
Tooth width, mm	49.1
Slot width, mm	21.1
Efficiency, %	52.90
Power factor	0.156
Primary weight, kg	250.8
Output thrust, N	505.7
Electromagnetic normal force, kN	11.1
Speed, m/s	20
Voltage, V	220

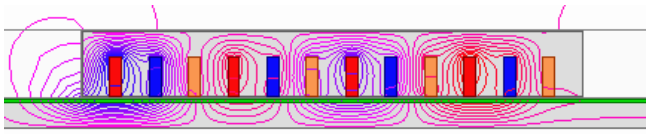

Fig. 3. Flux paths in the moving SLIM.

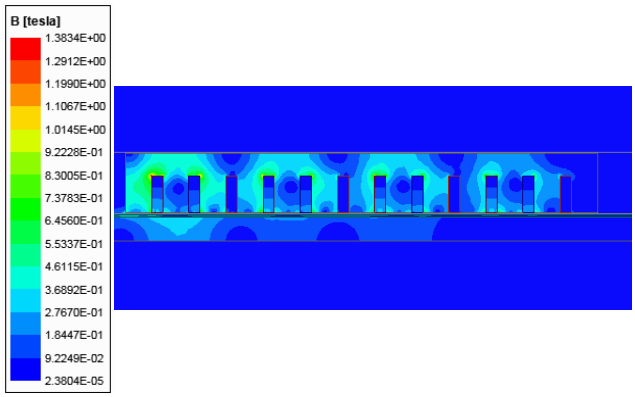

Fig. 4. Flux density distribution in different parts of the moving SLIM.

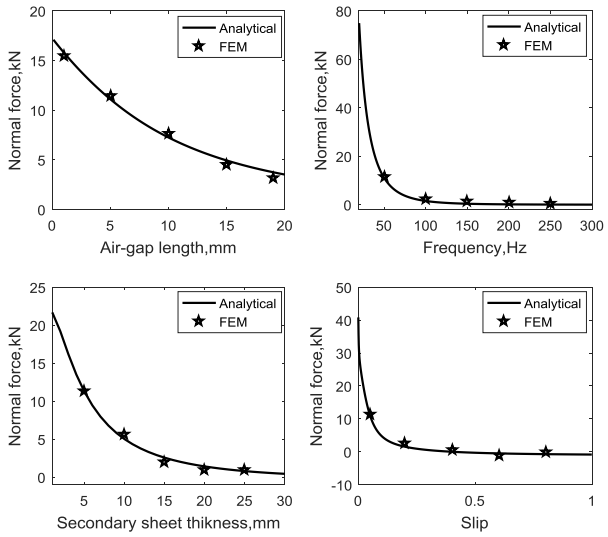

Fig. 5. Electromagnetic normal force versus motor parameters for designed SLIM.

A. Model Validation Through FEA

To confirm the mathematical equations presented in Sections II–IV and used for design optimization in the following, an example SLIM is considered with design data listed in Table I.

Figs. 3 and 4 illustrate the flux lines and flux density map obtained by 2-D FEA in rated operating conditions, respectively.

In Fig. 5, the electromagnetic normal force versus air-gap length, input frequency, secondary sheet thickness, and slip derived by analytical calculations for the example motor are compared against those obtained by FEA. In the figure, for each variable, FEA results are obtained at five points. It is seen that the analytical results are in good accordance with FEA simulations, confirming the accuracy of the mathematical calculation models presented above and subsequently used for design optimization purposes.

B. Sensitivity Analysis

The electromagnetic normal force exerted on SLIM is affected by different design variables. In this section, the effect of changing different variables in the design such as the thickness of the secondary sheet, length of the air-gap length, input frequency, and pole pairs are investigated with regard to the example SLIM whose design data and ratings are provided in Table I. In the following, while the effect of a single variable change is studied, the other variables are maintained constant.

In Fig. 6, SLIM electromagnetic normal force versus design parameters such as air-gap length, frequency, secondary sheet (aluminum) thickness, and slip are illustrated. For each of the design variable under consideration, the SLIM is designed following the procedure described in Section III, in particular by adjusting the number of turns per phase, which is constrained to be integer. This accounts for the discontinuous

$$B_x = \left[\frac{\sinh(\pi y/\tau)}{\sinh(\pi g_{ei}/\tau) - j\sigma_{ei} d\mu_0 s V_s \cosh(\pi g_{ei}/\tau)} - \frac{j\sigma_{ei} d\mu_0 s V_s \cosh(\pi y/\tau)}{\sinh(\pi g_{ei}/\tau) - j\sigma_{ei} d\mu_0 s V_s \cosh(\pi g_{ei}/\tau)}\right] \mu_0 J_m e^{j(\pi x/\tau - \omega_1 t)} \quad (24)$$

$$B_y = \left[\frac{-\sigma_{ei} d\mu_0 s V_s \sinh(\pi y/\tau)}{\sinh(\pi g_{ei}/\tau) - j\sigma_{ei} d\mu_0 s V_s \cosh(\pi g_{ei}/\tau)} - \frac{j\cosh(\pi y/\tau)}{\sinh(\pi g_{ei}/\tau) - j\sigma_{ei} d\mu_0 s V_s \cosh(\pi g_{ei}/\tau)}\right] \mu_0 J_m e^{j(\pi x/\tau - \omega_1 t)} \quad (25)$$

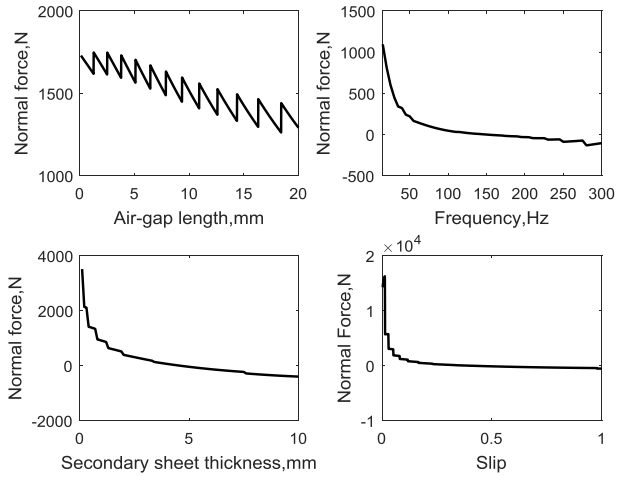

Fig. 6. Electromagnetic normal force versus SLIM design variables.

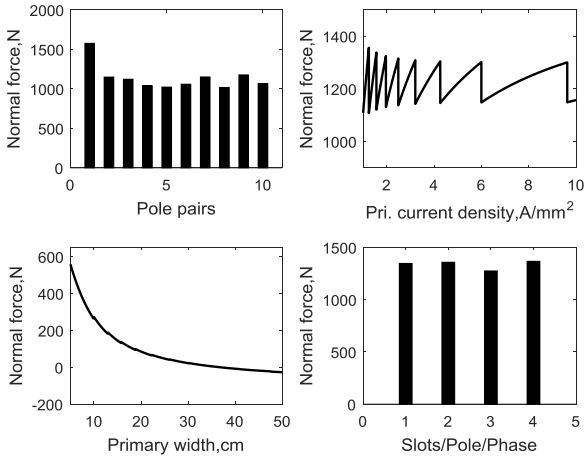

Fig. 7. Electromagnetic normal force versus SLIM design variables.

behavior (jumps) that can be observed in some of the diagrams reported.

In particular, it is seen in Fig. 6 that by increasing the air-gap length, the normal force decreases. Also, by increasing the input frequency at constant speed (20 m/s), the normal force decreases until it becomes negative at high frequencies. It means that the repulsion normal force is higher than the attraction one, at high frequencies. In addition, increasing both the thickness of the secondary sheet and the motor slip reduces the normal force. The normal force takes a negative value for large values of secondary sheet thickness and slip. The variations in the electromagnetic normal force versus the number of pole pairs, primary current density, primary width, and number of slots/pole/phase are shown in Fig. 7. As it can be seen, the number of slots/pole/phase does not have a remarkable effect, and the number of pole pairs and primary current density have low impact on the normal force (except for the $p = 1$ case), while increasing the primary width decreases the normal force.

Based on the obtained results, one can choose the design variables of the motor in such a way that it minimizes the electromagnetic normal force. In the next section, based on the obtained results and using genetic algorithm, the design variables of the motor are optimized to cancel out the normal force, in different conditions.

TABLE II
DESIGN VARIABLE CONSTRAINTS

Parameter	Minimum value	Maximum value
Current density, A/mm^2	3	6
Primary width, mm	40	500
Secondary sheet thickness, mm	1	10
Slip	0.05	0.5
Air-gap length, mm	5	20
Number of pole pairs	1	5
Frequency, Hz	10	200
Efficiency, %	30	-
Power factor	0.10	-

VI. OPTIMIZATION

Looking at Fig. 1(a) and (b), we can observe that three normal forces, namely, attraction ($F_{\rm ya}$), repulsion ($F_{\rm yr}$), and weight force ($F_{\rm yw}$), act on the primary, in different directions. In Fig. 1(a), the repulsion force is positive, while the attraction and weight forces are negative; in Fig. 1(b), the repulsion and weight forces are negative, while the attraction force is positive. In transportation applications, to facilitate the levitation of the vehicle, it is beneficial to cancel normal forces. In the following, the optimization is therefore performed in such a way that the resultant normal force acting on SLIM primary is driven to zero.

To optimize SLIM, different design variables can be chosen under design constraints. Considering the results of the sensitivity analysis presented in Section V, variables such as input frequency (f_1),number of pole pairs (p),primary current density (J_1),motor slip (s),primary width (W_s),thickness of the secondary conductive sheet (d), and air-gap length (g) are chosen as design variables. It should be mentioned that although the number of pole pairs and primary current density have low impact on the normal force, to increase the accuracy of the model and the studies, they are included in design optimization. The range of variation for each single design variable is reported in Table II.

The objective function is normal force minimization. For this purpose, however, design variables may be selected so that they increase the efficiency and power factor and reduce the primary weight. Therefore, efficiency, power factor, and primary weight should be included in the objective function. This is finally defined as follows:

$$f(x) = \frac{[\eta(\mathbf{x}) \times P.F.(\mathbf{x})]^{K_1}}{\left[\text{Primary weight}(\mathbf{x})\right]^{K_2} \times |F_y(\mathbf{x})|^{K_3} \times |F_{\rm yt}(\mathbf{x})|^{K_4}}. \tag{31}$$

In the above equation, x is the vector of design variables and $K_i (i = 1 \ldots 4)$ are constants which are chosen equal to either 0 or 1. $F_y(\boldsymbol{x})$ is the electromagnetic normal force which is defined in Section IV, and $F_{\rm yt}(\boldsymbol{x})$ is the total normal force acting on the primary, wherein the force due to the primary weight is included. For the situation in Fig. 1(a), the latter

TABLE III
OPTIMIZED MOTOR DATA IN DIFFERENT SCENARIOS

	Scenario 1 ($K_1=1, K_2=0$ $K_3=K_4=0$)	Scenario 2 ($K_1=K_2=1,$ $K_3=K_4=0$)	Scenario 3 ($K_1=K_2=1,$ $K3=1, K_4=0$)	Scenario 4 ($K_1=K_2=1,$ $K_3=0, K_4=1$)	Scenario 5 ($K_1=K_2=1,$ $K_3=0, K_4=1$)
Optimized quantities	• Efficiency • Power factor	• Efficiency • Power factor • Primary weight	• Efficiency • Power factor • Primary weight • E.m. normal force	• Efficiency • Power factor • Primary weight • Total normal force (Fig 1a)	• Efficiency • Power factor • Primary weight • Total normal force (Fig. 1b)
Primary current density, A/mm^2	3	6	5.9	5.4	3.9
Primary width, mm	500	103.7	368.8	174.2	157.0
Secondary sheet thickness, mm	1.2	1.3	4.5	7.9	3.4
Air gap length, mm	5.0	5.0	14.8	12.5	8
Slip	0.19	0.337	0.383	0.304	0.163
Number of pole pairs	5	2	2	3	4
Frequency, Hz	24.0	170.0	141.2	176.7	112
Number of turns per phase, N_1	165	84	54	51	128
Phase input current, A	28.6	57.4	88.6	185.5	63.3
Motor length (L_s), m	5.178	0.3747	0.4742	0.4969	0.8659
Tooth width, mm	34.2	3.1	14.8	9.2	13.0
Slot width, mm	23.0	7.2	23.4	17.9	22.5
Efficiency, %	69.38	56.47	53.33	60.39	73.08
Power factor	0.8409	0.4392	0.3249	0.1361	0.3341
Primary weight, kg	2405.5	18.18	70.38	49.69	71.33
Output thrust, N	549.85	470.21	506.45	503.07	510.40
Electromagnetic normal force, N	2722.9	1148.3	0.001	487.5	699.8
Total normal force, N	-20875.3	969.9	-690.5	-0.006	0.012
Objective function	0.5834	0.0136	2.4619	0.0016	0.0034

force is defined as follows:

$$F_{\mathrm{yt}}(x) = F_{\mathrm{yr}} - F_{\mathrm{ya}} - F_{\mathrm{yw}} \tag{32}$$

while for the situation in Fig. 1(b), $F_{\mathrm{yt}}(x)$ is defined by

$$F_{\mathrm{yt}}(x) = F_{\mathrm{ya}} - F_{\mathrm{yr}} - F_{\mathrm{yw}}. \tag{33}$$

In this article, genetic algorithm is used for optimization [35]. Using (31), optimization is performed for different objective functions. In a first scenario, $K_1 = 1$ and $K_2 = K_3 = K_4 = 0$ are chosen which leads to optimization of the efficiency and power factor. In a second scenario, $K_1 = K_2 = 1$ and $K_3 = K_4 = 0$ are chosen, so that, in addition to the efficiency and power factor, the primary weight is also optimized. In a third scenario, $K_1 = K_2 = K_3 = 1$ and $K_4 = 0$ are chosen, which means that in addition to the quantities considered in the second scenario, the electromagnetic normal force is also optimized. The fourth and fifth scenarios are similar to the third scenario; the only difference is that the total normal forces in Fig. 1(a) and (b) are chosen for optimization instead of the electromagnetic normal force; so, in both the scenarios $K_1 = K_2 = K_4 = 1$ and $K_3 = 0$. Thus, in the fourth scenario in addition to efficiency, power factor, and primary weight, the total normal force in the electromagnetic levitation system shown in Fig. 1(a) is optimized; finally, in the last scenario, the total normal force for the electrodynamic levitation system shown in Fig. 1(b) is optimized.

The results of the optimizations are summarized in Table III. The motor is designed to produce 500 ± 50 N at a speed of 20 m/s.

In the first design scenario, in which the efficiency and power factor are optimized, due to the fact that there is no limitation on the primary weight, the dimensions of the motor are large and the input frequency is comparatively low. Also, the primary current density is 3 A/mm^2, which leads to higher efficiency. In this case, the electromagnetic normal force is 2723 N. It is seen that the efficiency and the power factor have been improved from 52.9% and 0.156 for initial design to 69.4% and 0.84, respectively.

In the second scenario ($K_1 = K_2 = 1$, $K_3 = K_4 = 0$), the primary weight is optimized in addition to efficiency and power factor. As it is seen from the third column of Table III, the primary weight is 18.2 kg which is lower than that for the first scenario. In addition, the primary current density is 6 A/mm^2 which leads to reduced efficiency, in this case. Besides, the number of pole pairs is reduced to 2. Also, the power factor in this case is reduced compared with the first scenario.

In the next scenario ($K_1 = K_2 = K_3 = 1$, $K_4 = 0$), in which the absolute value of the electromagnetic normal force is optimized in addition to efficiency, power factor, and primary weight, the dimensions of the motor are comparatively small but larger than their counterparts in the second scenario. As seen in the fourth column of Table III, the normal force in this case is reduced approximately to zero ($F_y = 1$ mN). This means that the repulsion force between the primary and secondary aluminum sheet is canceled out by the attraction force between the primary and secondary back-iron. The convergence characteristic of the normal force for the third scenario is shown in Fig. 8. It is seen that the normal force converges to its final value of 1 mN within 400 iterations.

In the fourth scenario, the total normal force exerted on the primary in Fig. 1(a) is optimized in addition to efficiency,

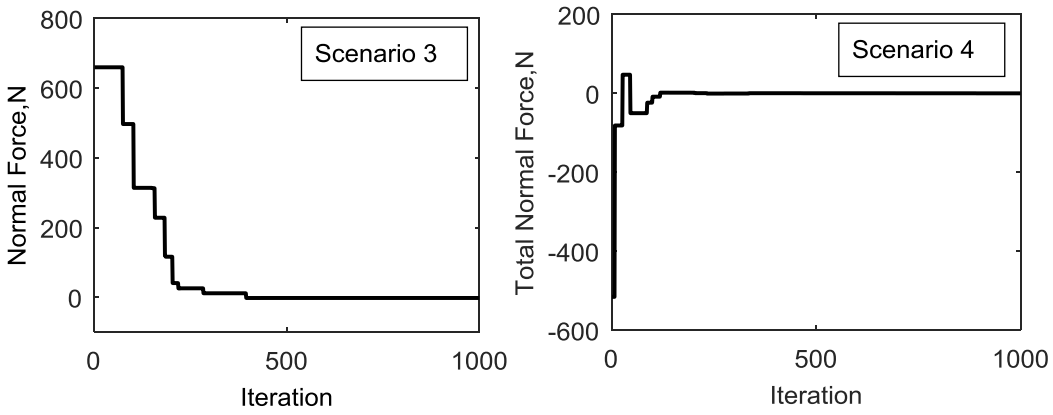

Fig. 8. Convergence characteristic of the normal force and total normal force for scenarios 3 and 4 of Table III, respectively.

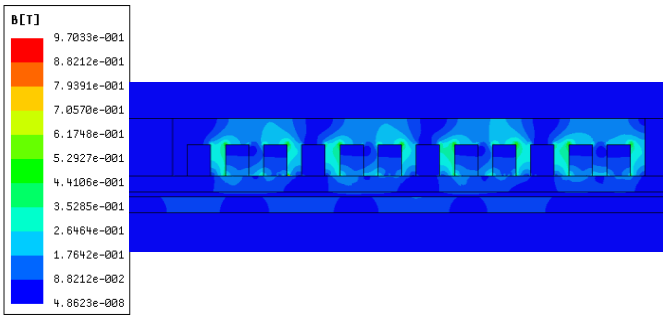

Fig. 9. Flux density distribution in different parts of the optimized SLIM (scenario 3).

power factor, and primary weight. As seen in the fifth column of Table III, the secondary sheet thickness is 7.9 mm, which is larger than those for previous scenarios. The high value of the secondary sheet thickness increases the repulsion normal force to compensate for the attraction normal force and the normal force component due to the primary weight. In addition, the magnetic air gap $(g + d)$ is 20.4 mm in this scenario. This high value of the magnetic air gap length deteriorates the performance of the motor. So, the efficiency and power factor are 60.4% and 0.136, respectively. Also, the normal force is -6 mN which means that the repulsion normal force cancels the attraction normal force and the normal force due to the primary weight. Fig. 8 illustrates the convergence characteristic of the total normal force for the fourth scenario.

Finally, in the last scenario, in addition to efficiency, power factor, and primary weight, the total normal force exerted on the primary in Fig. 1(b) is optimized. As seen in Fig. 1(b), the attraction normal force is positive and opposite to the repulsion normal force and the normal force caused by the primary weight. So, in this scenario, the secondary sheet thickness and the air-gap length are 3.4 and 8 mm, respectively, which are lower than those in scenarios 3 and 4. Also, the efficiency and power factor are 73.1% and 0.334, respectively, which are higher than the efficiency and power factor in scenario 4. The net normal force in this scenario is 12 mN. Comparing the results of scenarios 3–5, it is seen that scenario 5 gives better performance than the other two scenarios.

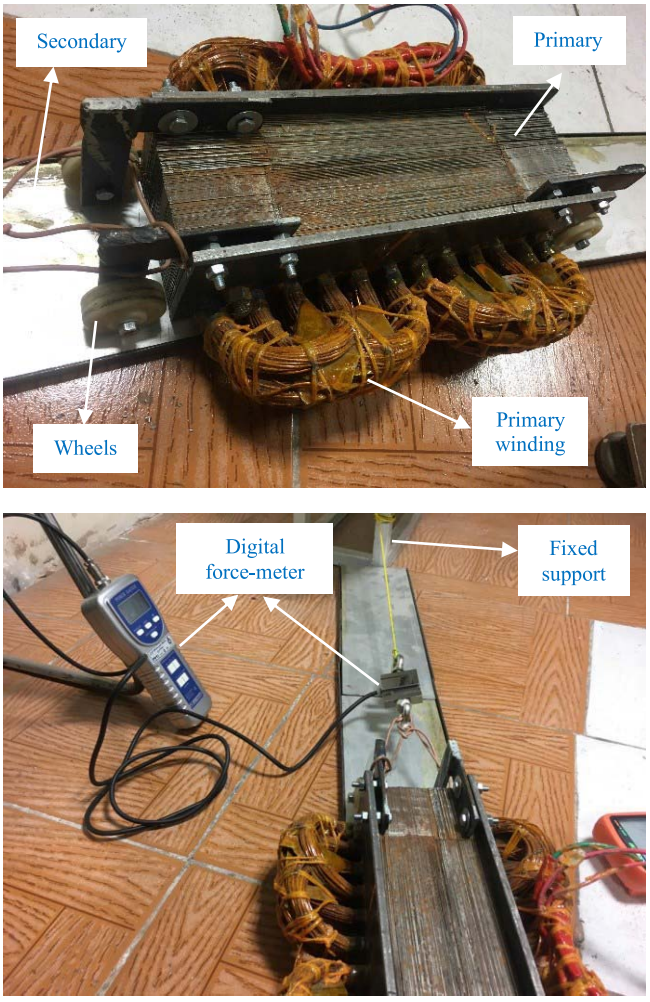

Fig. 10. Constructed motor and test setup.

So, in transportation applications, an SLIM structure like that shown in Fig. 1(b) may be recommended for levitation purposes. It should be mentioned that the normal force reported in columns 2–4 of Table III are the electromagnetic normal forces and columns 5 and 6 are the total normal force taking the normal force caused by the primary weight into account.

TABLE IV

COMPARISON OF THE CALCULATION AND FEA RESULTS

	Scenario 1		Scenario 2		Scenario 3		Scenario 4		Scenario 5	
Parameter	Analytical	FEM	Analytical	FEM	Analytical	FEM	Analytical	FEM	Analytical	FEM
Efficiency, %	69.4	67.1	56.5	54.0	53.3	50.9	60.4	57.9	73.1	70.5
Power factor	0.84	0.88	0.44	0.45	0.33	0.35	0.14	0.15	0.33	0.35
Normal force, N	2722.9	2682.3	1148.3	1194.7	0.001	0.041	487.5	472.5	699.8	708.6
Thrust, N	549.9	567.6	470.2	488.3	506.5	512.8	503.1	525.8	510.4	526.7

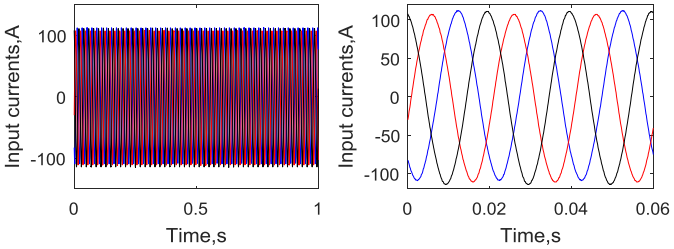

Fig. 11. Locked-primary input currents for input voltage of 78.57 V.

VII. VALIDATION

To confirm the optimization results, FEA and test results are used as explained below.

A. FEA Simulations

To validate the optimization results, the optimized motors given in Table III are simulated using 2-D FEM. Flux density distribution in different parts of the optimized motor of scenario 3 is illustrated in Fig. 9, for instance. Fig. 9 shows that the maximum value of the flux density in different parts of the optimized motor is below 1 T. Also, the flux density in the air gap and the secondary sheet does not exceed 0.2 T. This low value is due to the large elecntromagnetic air-gap length (14.8 + 4.5 mm) in the optimized design. The efficiency, power factor, thrust, and normal force are calculated using FEA simulations. The FEA results are compared with analytical calculations in Table IV. It is observed in this table that the efficiencies obtained analytically are higher than those obtained by FEA. This is a consequence of neglecting iron losses in the analytical model, while they are included in FEA simulations. Also, the differences between the power factors obtained by two methods are due to edge effects which are considered in analytical calculations but not in FEA. Instead, the normal forces and thrusts obtained by FEA are very close to the analytical estimations, confirming the validity of the proposed modeling for design and optimization.

B. Experimental Results

For the purpose of further validation, the designed motor given in the fourth column of Table III (scenario 3) has been constructed and tested. Due to space limitations in the laboratory, the length of the secondary rail is limited to 2 m.

Fig. 10 shows the motor and test setup. Considering the nominal speed of 18.65 m/s, the motor cannot reach the steady-state operation in 2-m rail. Thus, the tests have been performed in locked-primary conditions ($s = 1$) under 50-Hz network

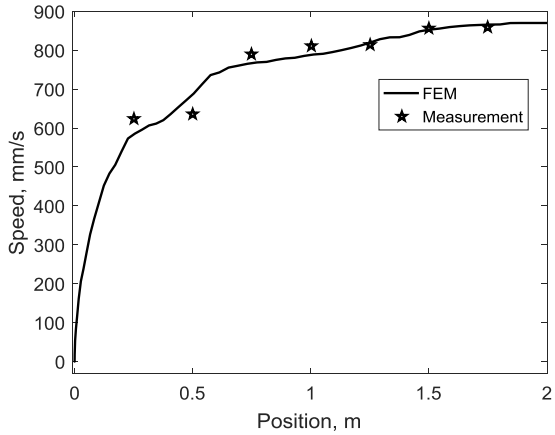

Fig. 12. Speed of the motor versus position (input frequency is 4 Hz).

TABLE V

COMPARISON OF THE CALCULATION AND EXPERIMENTAL RESULTS AT STARTING

Input voltage, V	Input current, A		Thrust, N		Electromagnetic normal force, N	
	Calc.	Test	Calc.	Test	Calc.	Test
100	103.65	106.3	896.13	880.6	98.09	97.1
78.57	81.44	84.0	553.22	543.4	60.56	57.8
50	51.82	53.8	224.03	217.8	24.52	23.4
30	31.09	32.1	80.65	76.9	8.83	8.1
20	20.73	21.7	35.85	33.6	3.92	3.4

frequency. So, the input frequency is also set equal to 50 Hz in calculations. Fig. 11 shows the measured three-phase locked-primary input currents for an input voltage of 78.6 V. It is seen that the amplitude of phase *b* is lower than the amplitude of the other phases. This is because of the static end-effect phenomenon. The phase *a* input current, thrust, and normal force have been measured for different voltages lower than the nominal value of 220 V. The forces have been measured by a digital force-meter "Lutron FG-5100" connected to a computer via serial port. The results are reported and compared with calculations in Table V.

As can be seen in the table, the calculated input currents are close to the measured values. The maximum error (6.1%) is related to the current which has been obtained for an input voltage of 20 V. Other errors of the input currents are less than 5%. It is also observed that the calculated starting thrusts and the normal forces for different voltages are in good accordance

with the measured ones, confirming the analytical calculations and optimization method.

To check the transient behavior of the built prototype, the speed of the machine has been measured and plotted versus time, during starting in no-load conditions. Also, the measured speeds at different positions are compared with those obtained by FEA. As mentioned before, the length of the rail in the laboratory is 2 m. So, to reach the steady-state condition in 2 m, the input frequency and the input voltage are decreased to 4 Hz and 20 V, respectively.

To measure the speed, Atmega16 microcontroller, TRCT5000 infrared module, and LM2596 dc–dc step down regulator are used. In Fig. 12, the transient speed of the motor versus position obtained by FEA is illustrated. It is seen in this figure that the motor reaches the steady-state value of 0.87 m/s in 2-m rail. The difference between this speed and synchronous speed (0.92 m/s) is due to the friction between the rail and the motor wheels. Also, the motor speeds in different positions are measured and compared with FEA results in Fig. 12. It is observed that the results of the measurement are in good accordance with FEA results, especially for high speeds.

VIII. Conclusion

Analytical expressions for the attraction and repulsion normal forces acting on the primary and sencondary of an SLIM have been derived from the Maxwell electromagnetic field equations. The effects of different design variables on such forces have been investigated. A multi-objective design optimization method is usend to minimize the primary weight and normal force of an SLIM, in addition to improving the efficiency and power factor. The results show that the normal force with and without considering the primary weight can be effectively canceled by appropriate selection of the design variables. Optimization results have been presented and discussed considering different design scenarios, differing by the targets assumed and the SLIM arrangement being considered. As a validation, an optimized motor design is simulated using 2-D FEA in rated conditions and also implemented into a physical prototype which has been tested in locked-primary conditions and during starting. The results of both FEA simulations and experiments are in good accordance with analytical predictions demonstrating the accuracy of the SLIM analytical model and the optimization results obtained through it.

Given the importance of minimizing normal force in SLIM applications to vehicle traction, this article can be a useful reference for a computationally efficient machine optimization based on easy-to-handle but sufficiently accurate analytical equations.

References

[1] I. Boldea and S. A. Nasar, *Linear Motion Electromagnetic Devices*. New York, NY, USA: Taylor & Francis, 2001.

[2] R. C. Creppe, J. A. C. Ulson, and J. F. Rodrigues, "Influence of design parameters on linear induction motor end effect," *IEEE Trans. Energy Convers.*, vol. 23, no. 2, pp. 358–362, Jun. 2008.

[3] S. Nonaka, "Investigation of equations for calculation of secondary resistance and secondary leakage reactance of single-sided linear induction motors," *Electr. Eng. Jpn.*, vol. 122, no. 1, pp. 60–67, Jan. 1998.

[4] E. R. Laithwaite and S. A. Nasar, "Linear-motion electrical machines," *Proc. IEEE*, vol. 58, no. 4, pp. 531–542, Apr. 1970.

[5] H. Heidari *et al.*, "A modified dynamic model of single-sided linear induction motors considering longitudinal and transversal effects," *Electronics*, vol. 10, no. 8, p. 933, Apr. 2021.

[6] S.-B. Yoon, J. Hur, and D.-S. Hyun, "A method of optimal design of single-sided linear induction motor for transit," *IEEE Trans. Magn.*, vol. 33, no. 5, pp. 4215–4217, Sep. 1997.

[7] W. Xu, J. Zhu, L. Tan, Y. Guo, S. Wang, and Y. Wang, "Optimal design of a linear induction motor applied in transportation," in *Proc. IEEE Int. Conf. Ind. Technol.*, Feb. 2009, pp. 1–6.

[8] Y. He, Y.-S. Wang, Q. Lu, L. Zhang, and F. Liang, "Design of single-sided linear induction motor for low-speed maglev vehicle in 160 km/h and variable slip frequency control," *Transp. Syst. Technol.*, vol. 4, no. 2, pp. 120–128, Sep. 2018.

[9] Y. Ying, D. Jiangmin, T. Laisheng, L. Xiaochun, P. Qibiao, and Z. Wenhui, "Study on the optimization of linear induction motor traction system for fast-speed maglev train," *Transp. Syst. Technol.*, vol. 4, no. 3, pp. 156–164, 2018.

[10] S. Osawa, M. Wada, M. Karita, D. Ebihara, and T. Yokoi, "Light-weight type linear induction motor and its characteristics," *IEEE Trans. Magn.*, vol. 28, no. 5, pp. 3003–3005, Sep. 1992.

[11] M. Kitamura, N. Hino, H. Nihei, and M. Ito, "A direct search shape optimization based on complex expressions of 2-dimensional magnetic fields and forces," *IEEE Trans. Magn.*, vol. 34, no. 5, pp. 2845–2848, Sep. 1998.

[12] B. Laporte, N. Takorabet, and G. Vinsard, "An approach to optimize winding design in linear induction motors," *IEEE Trans. Magn.*, vol. 33, no. 2, pp. 1844–1847, Mar. 1997.

[13] A. H. Isfahani, B. M. Ebrahimi, and H. Lesani, "Design optimization of a low-speed single-sided linear induction motor for improved efficiency and power factor," *IEEE Trans. Magn.*, vol. 44, no. 2, pp. 266–272, Feb. 2008.

[14] C. Lucas, Z. Nasiri-Gheidari, and F. Tootoonchian, "Application of an imperialist competitive algorithm to the design of a linear induction motor," *Energy Convers. Manage.*, vol. 51, no. 7, pp. 1407–1411, Jul. 2010.

[15] A. Z. Bazghaleh, M. R. Naghashan, and M. R. Meshkatoddini, "Optimum design of single-sided linear induction motors for improved motor performance," *IEEE Trans. Magn.*, vol. 46, no. 11, pp. 3939–3947, Nov. 2010.

[16] A. Shiri and A. Shoulaie, "End effect braking force reduction in high-speed single-sided linear induction machine," *Energy Convers. Manage.*, vol. 61, pp. 43–50, Sep. 2012.

[17] J. H. Jeong, J. W. Lim, D. Y. Park, J. Y. Choi, and S. M. Jang, "Characteristic analysis of a linear induction motor for 200-km/h Maglev," *Int. J. Railway*, vol. 8, no. 1, pp. 15–20, Mar. 2015.

[18] J. Lim, J.-H. Jeong, C.-H. Kim, C.-W. Ha, and D.-Y. Park, "Analysis and experimental evaluation of normal force of linear induction motor for maglev vehicle," *IEEE Trans. Magn.*, vol. 53, no. 11, pp. 1–4, Nov. 2017.

[19] B.-T. Ooi and D. White, "Traction and normal forces in the linear induction motor," *IEEE Trans. Power App. Syst.*, vol. PAS-89, no. 4, pp. 638–645, Apr. 1970.

[20] E. M. Freeman and D. A. Lowther, "Normal force in single-sided linear induction motors," *IEE Proc.*, vol. 120, no. 12, pp. 1499–1506, Dec. 1973.

[21] L. Shi, H. Zhang, and K. Wang, "Analysis of forces in combined levitation- and-propulsion SLIM system," in *Proc. IEEE Int. Conf. Elect. Mach. Syst.*, Oct. 2008, pp. 2960–2963.

[22] Z. Yang, J. Zhao, and T. Q. Zheng, "A novel traction and normal forces study for the linear induction motor," in *Proc. Int. Conf. Elect. Mach. Syst.*, Oct. 2008, pp. 3474–3477.

[23] A. A. Kuijpers, C. Nemlioglu, F. Sahin, A. Verdel, J. C. Compter, and E. A. Lomonova, "Force analysis of linear induction motor for magnetic levitation system," in *Proc. 14th Int. Power Electron. Motion Control Conf. (EPE-PEMC)*, Sep. 2010, pp. 3–17.

[24] G. Kaminski, W. Przyborowski, P. Staszewski, A. Biernat, and E. Kupiek, "Design and test results of laboratory model of linear induction motor for automation personal urban transport PRT," *Przeglad Elektrotechniczny*, vol. 93, no. 3, pp. 276–283, 2017.

[25] L. Bin, F. Jin, C. Junci, C. Jie, S. Hang, and S. Long, "Electromagnetic performance calculation of HTS linear induction motor for rail systems," *J. Phys., Conf.*, vol. 871, Jul. 2017, Art. no. 012097.

[26] A. Z. Bazghaleh and E. F. Choolabi, "A new approach for non-linear time-harmonic FEM-based analysis of single-sided linear induction motor incorporated with a new accurate method of force calculation," *IEEE Trans. Magn.*, vol. 57, no. 2, pp. 1–9, Feb. 2021.
[27] J. A. D. Hernández, N. D. Carralero, and E. G. Vázquez, "A 3-D simulation of a single-sided linear induction motor with transverse and longitudinal magnetic flux," *Appl. Sci.*, vol. 10, no. 19, p. 7004, Oct. 2020.
[28] F. N. Sarapulov, V. E. Frizen, E. L. Shvydkiy, and I. A. Smol'yanov, "Mathematical modeling of a linear-induction motor based on detailed equivalent circuits," *Russian Electr. Eng.*, vol. 89, no. 4, pp. 270–274, Jun. 2018.
[29] H. Seo, J. Lim, G.-H. Choe, J.-Y. Choi, and J.-H. Jeong, "Algorithm of linear induction motor control for low normal force of magnetic levitation train propulsion system," *IEEE Trans. Magn.*, vol. 54, no. 11, pp. 1–4, Nov. 2018.
[30] J. Duncan, "Linear induction motor-equivalent circuit model," *IEE Proc. Electr. Power Appl.*, vol. 130, no. 1, pp. 51–57, Jan. 1983.
[31] W. Xu, J. G. Zhu, Y. Zhang, Y. Li, Y. Wang, and Y. Guo, "An improved equivalent circuit model of a single-sided linear induction motor," *IEEE Trans. Veh. Technol.*, vol. 59, no. 5, pp. 2277–2289, Jun. 2010.
[32] W. Xu *et al.*, "Equivalent circuits for single-sided linear induction motors," *IEEE Trans. Ind. Appl.*, vol. 46, no. 6, pp. 2410–2423, Nov./Dec. 2010.
[33] A. Shiri and A. Shoulaie, *Linear Induction Motors, Analysis, Design and Modelling*, Tehran, Iran: Shahid Rajaee Univ. Press, 2016.
[34] D. K. Cheng, *Field and Wave Electromagnetics*. Boston, MA, USA: Edison Wesley, 1983.
[35] S. Sumathi and P. Surekha, *Computational Intelligence Paradigms: Theory and Applications Using MATLAB*. New York, NY, USA: CRC Press, 2010.

Abbas Shiri (Member, IEEE) received the B.Sc. degree from Tabriz University, Tabriz, Iran, in 2004, and the M.Sc. and Ph.D. degrees from the Iran University of Science and Technology, Tehran, Iran, in 2006 and 2013, respectively, all in electrical engineering.

He is currently an Assistant Professor with Shahid Rajaee Teacher Training University, Tehran. His research interests include linear electric machines, electromagnetic systems and actuators, and electrical machine design and modeling.

Alberto Tessarolo (Senior Member, IEEE) received the Laurea degree in electrical engineering from the University of Padua, Padua, Italy, in 2000, and the Ph.D. degree in electrical engineering from the University of Trieste, Trieste, Italy, in 2011.

Before joining the University, he worked in the industry in the design and development of large innovative motors, generators and drives. Since 2006, he has been with the Department of Engineering and Architecture, University of Trieste, where he currently teaches the courses in electric machine fundamentals and electric machine design as a Full Professor. He has authored over 180 international articles in areas of electrical machines and drives.

Dr. Tessarolo has served as an Associate Editor for IEEE TRANSACTIONS ON INDUSTRY APPLICATIONS and *IET Electric Power Applications* from 2016 to 2021. He is also the Editor-in-Chief of IEEE TRANSACTIONS ON ENERGY CONVERSION.